3D Higher-Order X-FEM Model for the Simulation of Cohesive Cracks in Cementitious Materials Considering Hygro-Mechanical Couplings

C. Becker[1], S. Jox[2] and G. Meschke[3]

Abstract: A three-dimensional numerical model based on the Extended Finite Element Method (X-FEM) is presented for the simulation of cohesive cracks in cementitious materials, such as concrete, in a hygro-mechanical framework. Enhancement functions for the small scale resolution of the displacement jump across cracks in the context of the X-FEM is used in conjunction with a higher order family of hierarchical shape functions for the representation of the large scale displacement field of the investigated structure. Besides the theoretical and computational formulation in a multiphase context, aspects of the implementation, such as integration and crack tracking algorithms, are discussed. Representative numerical examples include 3D benchmark problems, an analysis of anchor pullout test and an application of the model to a hygro-mechanically loaded concrete beam.

Keywords: 3D-X-FEM; cracking; concrete structures; hygro-mechanical coupling; porous materials

1   Introduction

Realistic modeling of the opening and propagation of cracks is a prerequisite for reliable prognoses of the serviceability, safety and durability of concrete, reinforced concrete and masonry structures. In the context of lifetime-oriented design, consideration of changing hygro-thermal environmental conditions including the transport of moisture within opening cracks and the respective hygro-mechanical couplings (Coussy and Ulm (2001)) is essential. Information on the width and topology of evolving cracks is crucial, since crack widths exceeding a certain critical crack opening may considerably promote the transport of corrosive substances (Maekawa

[1] Institute for Continuum Mechanics, Ruhr-University Bochum, Germany, *becker@lkm.rub.de*
[2] ZERNA Ingenieure GmbH, Bochum, Germany, *jox@zerna.eu*
[3] Corresponding Author, Institute for Structural Mechanics, Ruhr-University Bochum, Germany, *guenther.meschke@rub.de*

and Ishida (2002)) when filled with water. Up to the mid of the 1990's research in computational failure analysis of concrete and reinforced concrete structures was focussed on two alternative approaches: continuum-based models (see the reviews contained e.g. in de Borst (2002); Mang, Meschke, Lackner, and Mosler (2003)) and discrete representations of fracture along mesh boundaries using concepts of Linear Elastic Fracture Mechanics (LEFM) and cohesive crack models (see, e.g., Ingraffea and Saouma (1985); Xie and Gerstle (1995)). Since the mid of the 1990's, the goal of a discrete representation of cracks within the framework of the Finite Element Method has resulted in approaches to represent cracks as embedded discontinuities within finite elements, circumventing the need for re-meshing as cracks evolve. From a conceptual point of view, this strategy has the character of multiscale methods, characterized by superimposing the small scale resolution (the displacement jump across cracks) onto a large scale resolution of the (smooth) displacement field.

These formulations can generally be categorized into element-based formulations, generally denoted as Embedded Crack Models (see Simo, Oliver, and Armero (1993); Oliver (1996); Jirásek and Zimmermann (2001); Armero and Garikipati (1996); Mosler and Meschke (2003), among others), and nodal-based formulations, i.e. the Extended Finite Element Method (*X*-FEM) (see Moës, Dolbow, and Belytschko (1999); Moës and Belytschko (2002); Wells and Sluys (2001a)). For a comparative assessment of both approaches we refer to Jirásek and Belytschko (2002); Dumstorff, Mosler, and Meschke (2003). The Extended Finite Element Method has been successfully applied to model traction-free cracks in the context of the LEFM in two- and three-dimensional settings (see. e.g. Moës, Dolbow, and Belytschko (1999); Belytschko, Möes, Usui, and Parimi (2001); Sukumar, Moës, Moran, and Belytschko (2000)) as well as for cohesive cracks (e.g. Wells and Sluys (2001b); Moës and Belytschko (2002); Mariani and Perego (2003); Zi and Belytschko (2003); Mergheim, Kuhl, and Steinmann (2005); Dumstorff and Meschke (2007)). Since the topology of cracks is held fixed once they are signaled to open, the determination of the crack propagation direction and of the crack path has received considerable attention (see Oliver and Huespe (2002); Feist and Hofstetter (2006); Meschke and Dumstorff (2007); J ager, Steinmann, and Kuhl (2008)).

In recent years the Extended Finite Element Method has been successfully applied to fully three-dimensional problems (Sukumar, Moës, Moran, and Belytschko, 2000; Moës, Sukumar, Moran, and Belytschko, 2000; Sukumar, Chopp, and Moran, 2003; Gasser and Holzapfel, 2005). Considering 3D implementations of the *X*-FEM, in general a conflict between accuracy, applicability and the complexity of the numerical implementation arises, since, compared to 2D implementations, the effort increases considerably. In particular, with respect to crack tracking algorithms, the

problem changes from the determination of the crack propagation angle Θ_c and the crack propagation length $\triangle l_c$ initiating from the current crack tip to the determination of the three-dimensional evolution of crack surfaces emanating from (non-smooth) crack fronts. While the geometry of the evolving crack can be easily described explicitly in two-dimensional formulations, for the description of the crack topology and crack propagation in three-dimensional implementations often use of implicit strategies based on the level set method (Osher and Sethian, 1988; Osher and Fedkiw, 2003) is made. In (Moës, Gravouil, and Belytschko, 2002; Gravouil, Moës, and Belytschko, 2002) the *level-set method* is used to represent arbitrary crack growth by solving HAMILTON-JACOBI-type equations.

In the majority of existing 3D implementations of the *X*-FEM for crack propagation analyses tetrahedral elements with linear approximations of the displacement field are used in combination with elementwise plane crack propagation (see e.g. (Areias and Belytschko, 2005)). In the present paper, a 3D *X*-FEM model is formulated within the framework of a higher-order Finite element formulation (p-FEM) (Becker, Jox, and Meschke, 2009). Both *X*-FEM and p-FEM are characterized by the improvement of the approximation quality by adding higher order functions to the linear approximation. The combination of *X*-FEM and p-FEM allows to adapt the large scale resolution to the type of problem at hand using (anisotropic) higher order shape functions, while the discontinuous approximations added in the *X*-FEM allow for the resolution of the displacement field at the scale of the crack. This discretization concept is formulated in a generalized, hygro-mechanical framework considering the influence of cracks on the liquid permeability of concrete (Barton, Bandis, and Bakhtar (1985); Meschke and Grasberger (2003)). For the hygro-mechanical formulation in a continuum setting, the Theory of Porous Media (TPM) (Coussy (1989); Schrefler (1995)) is used (see Grasberger and Meschke (2004); Meschke and Grasberger (2003)). In this framework, the effect of cracks on the moisture transport is considered using the information on the crack width and crack topology from the *X*-FEM model.

The remainder of the paper is organized as follows: Section 2 contains a review of the Extended Finite Element Method in a 3D setting. In Section 3 the hierarchical higher order concept used for the field- and geometry-specific approximation of the field variables is presented. The extension to hygro-mechanically coupled analyses is contained in Section 4. Section 5 is devoted to the discussion of computational aspects such as the spatial integration of the 3D *X*-FEM model considering moisture transport within the crack channel. Finally, representative numerical examples for 3D single and multiphase crack analyses of concrete structures are presented in Section 6.

2   X-FEM resolution of displacement jumps across cracks

This section contains a summary of the Extended Finite Element Method in a 3D setting, restricted to the geometrically linear theory. It is assumed that cracks fully penetrate through elements. Consequently, no crack tip enhancements as proposed e.g. in Zi and Belytschko (2003); Asferg, Poulsen, and Nielsen (2005) are considered. For a more elaborate discussion on the background of the *X*-FEM we refer to Moës, Dolbow, and Belytschko (1999); Sukumar, Moës, Moran, and Belytschko (2000).

2.1   *Kinematics*

To incorporate a small scale resolution of the displacement jump across cracks into the finite element we start by decomposing the displacement field into a continuous part $\bar{\mathbf{u}}$ and discontinuous part $\check{\mathbf{u}}$ (see Figure (1)):
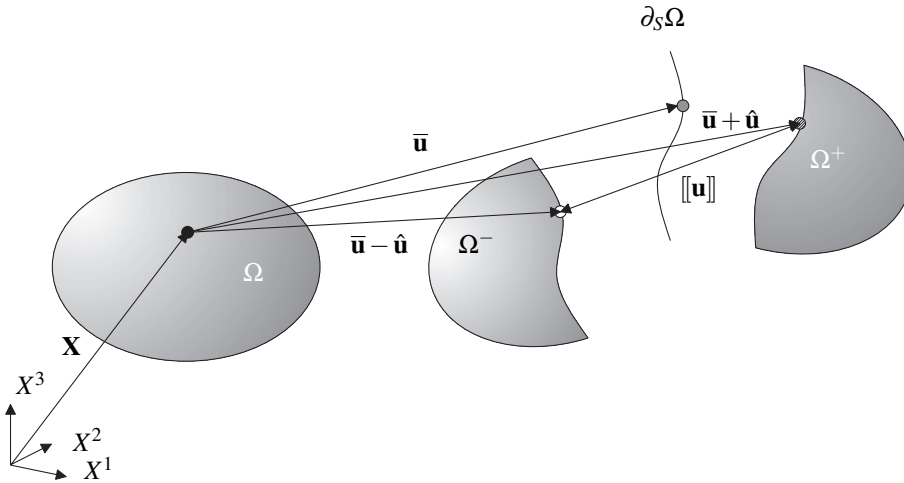

Figure 1: Separation of a body Ω by a discontinuity $\partial_S\Omega$ into subdomains Ω^- and Ω^+

$$\mathbf{u}(\mathbf{X}) = \bar{\mathbf{u}}(\mathbf{X}) + \check{\mathbf{u}}(\mathbf{X}). \tag{1}$$

The discontinuous part is described with the help of the SIGNUM function

$$S_S(\mathbf{X}) = \begin{cases} -1 & \forall \quad \mathbf{X} \in \Omega^- \\ 0 & \forall \quad \mathbf{X} \in \partial_S\Omega \\ 1 & \forall \quad \mathbf{X} \in \Omega^+ \end{cases} \tag{2}$$

which is multiplied with the enhanced regular part of the displacements $\hat{\mathbf{u}}$:

$$\check{\mathbf{u}}(\mathbf{X}) = S_S(\mathbf{X})\,\hat{\mathbf{u}}(\mathbf{X}). \tag{3}$$

With the SIGNUM function the displacement jump at the discontinuity can be expressed as

$$[\![\mathbf{u}]\!] = 2\,\hat{\mathbf{u}}(\mathbf{X})\Big|_{\mathbf{X}\in\partial_S\Omega}. \tag{4}$$

From taking the gradient of the displacement field (1) a continuum-related part of the strain field and a portion associated with the discontinuity containing the DIRAC-delta function δ_S is obtained:

$$\nabla\mathbf{u}(\mathbf{X}) = \nabla\bar{\mathbf{u}}(\mathbf{X}) + S_S(\mathbf{X})\,\nabla\hat{\mathbf{u}} + 2\,\delta_S\,[\hat{\mathbf{u}}(\mathbf{X})\otimes\mathbf{n}]. \tag{5}$$

2.2 *Weak form of balance of momentum including a discontinuity*

Incorporating the discontinuous displacement field (1) in the weak form of the balance of momentum

$$\int_\Omega \delta\nabla\mathbf{u} : \pm\sigma\,dV = \int_{\Gamma_\sigma} \delta\bar{\mathbf{u}}\,\mathbf{t}^\star\,d\Gamma_\sigma. \tag{6}$$

leads to

$$\int_\Omega [\delta\nabla\bar{\mathbf{u}} + S_S\,\delta\nabla\hat{\mathbf{u}}] : \pm\sigma\,dV + 2\int_\Omega \delta_S\,[\delta\hat{\mathbf{u}}\otimes\mathbf{n}] : \pm\sigma\,dV = \int_{\Gamma_\sigma} \delta\bar{\mathbf{u}}\,\mathbf{t}^\star\,d\Gamma_\sigma. \tag{7}$$

With the definition of an enhanced strain tensor

$$\pm\bar{\varepsilon} = \mathbf{B}\,\mathbf{u} = \mathbf{B}\,\bar{\mathbf{u}} + S_S\,\mathbf{B}\,\hat{\mathbf{u}}, \tag{8}$$

and the volume integral of the DIRAC-delta function

$$\int_\Omega \delta_S\,d\Omega = \int_{\partial_S\Omega} 1\,dA \tag{9}$$

finally the weak form of balance of momentum including a surface of discontinuity is obtained:

$$\int_\Omega \delta\pm\bar{\varepsilon} : \pm\sigma\,dV + 2\int_{\partial_S\Omega} \delta\hat{\mathbf{u}}\,\underbrace{\pm\sigma\,\mathbf{n}}_{\mathbf{t}_S}\,dA = \int_{\Gamma_\sigma} \delta\bar{\mathbf{u}}\,\mathbf{t}^\star\,d\Gamma_\sigma. \tag{10}$$

In Eq.(10) $\mathbf{t}_S$ is the traction vector acting on the surface of discontinuity which satisfies the balance of tractions:

$$[\![\mathbf{t}_S]\!] = \mathbf{0}, \quad \forall \mathbf{X} \in \partial_S \Omega. \tag{11}$$

A new crack is assumed to open if the average principal stress in an element exceeds the tensile strength (see Section 5). The transition from a gradual opening of a zone of micro-cracks to a fully developed macro-crack in concrete is represented by a cohesive zone model. Since in this paper the focus is laid on mode-I crack opening, the adopted softening interface law relates crack openings and tractions $\mathbf{t}_S$ in the direction of the crack normal $\mathbf{n}$ (see Figure(2)):

$$\mathbf{t}_S = t_n([\![\mathbf{u}]\!])\,\mathbf{n}. \tag{12}$$

This mode-I cohesive interface law is obtained as a special case of the mixed mode interface law proposed by Camacho and Ortiz (1996) by defining the equivalent displacement jump as the displacement jump in the normal direction:

$$t_n = t_n([\![u^{eq}]\!]), \quad [\![u^{eq}]\!] = \sqrt{[\![\mathbf{u}]\!]_n^2} = \|[\![\mathbf{u}]\!]_n\|. \tag{13}$$
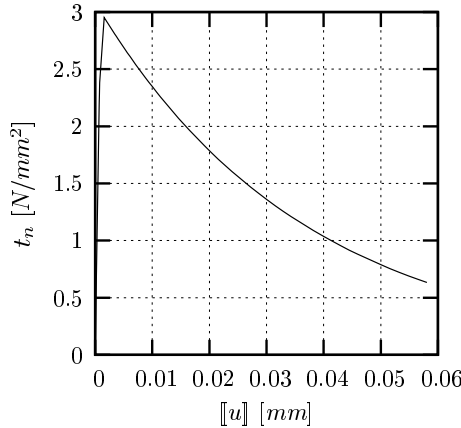

Figure 2: Interface law: softening relation between normal tractions and crack separation

Adopting concepts of damage theory, the relation between normal tractions and crack openings is given as Wells and Sluys (2001b):

$$t_n = \left[T - T^{da}([\![u^{eq}]\!])\right] [\![u^{eq}]\!], \tag{14}$$

with the initial stiffness T and the damaging (softening) portion T^{da} depending on the displacement jump:

$$T^{da} = T \left[1 - \frac{\alpha}{[\![u^{eq}]\!]} \exp\{ -\frac{f_{tu}}{G_f} [\![u^{eq}]\!] - \alpha_0]\} \right]. \tag{15}$$

In Eq.(15), α is the largest value of $[\![u^{eq}]\!]$ experienced in the loading history according to the damage criterion

$$\Phi([\![u^{eq}]\!], \alpha) = [\![u^{eq}]\!] - \alpha \leq 0, \tag{16}$$

f_{tu} is the tensile strength and G_f the fracture energy of concrete.

3 Hierarchical higher order approximation of smooth displacement fields

While the enhanced approximations of the displacement field according to the *X-FEM* is used for the resolution of the displacement field at the scale of the individual crack zones, a higher-order, anisotropic spatial discretization concept (p-FEM) as recently proposed in Becker, Jox, and Meschke (2009) for multifield problems is used for the resolution of the displacement at the large scale to allow for the adaption of the spatial resolution to the specific characteristics of the problem such as the geometry and to the requirements of the field variables involved, e.g. in coupled hygro-mechanical analyses.

The spatial discretization method is based on the hierarchically organized LEGENDRE polynomials. The one-dimensional shape functions can be easily generated by a recursive formula, see e.g. Szabó and Babuška (1991). The extension of the 1D hierarchical concept of LEGENDRE-based shape functions to three-dimensional shape functions for brick-type finite elements requires the numbering of relevant geometrical entities, such as nodes, edges and faces (Figure 3) (see Szabó and Babuška (1991); Düster (2002); Becker, Jox, and Meschke (2009)). The three-dimensional shape functions are obtained as products of the one-dimensional shape functions:

$$N_l^{3D}(\xi) = N_i^{1D}(\xi^1) \cdot N_j^{1D}(\xi^2) \cdot N_k^{1D}(\xi^3) \qquad \begin{array}{rcl} i & \in & \{1,2,3,...,p_{\xi^1}+1\} \\ j & \in & \{1,2,3,...,p_{\xi^2}+1\} \\ k & \in & \{1,2,3,...,p_{\xi^3}+1\} \\ l & \in & \{1,2,3,...,NN^{3D}\} \end{array}, \tag{17}$$

with the total number of element nodes

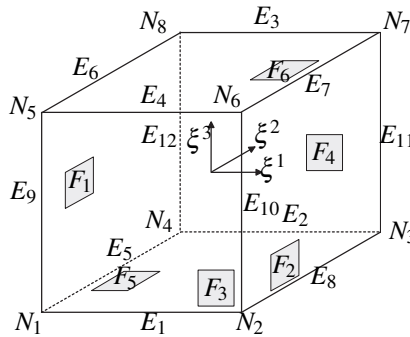$$NN^{3D} = [p_{\xi^1}+1] \cdot [p_{\xi^2}+1] \cdot [p_{\xi^3}+1]. \tag{18}$$

Figure 3: 3D-higher order element concept: Numbering of vertices (N_i), edges (E_i) and faces (F_i)

p_{ξ^i} represents the polynomial degree of approximation in the direction of the respective natural element coordinate ξ^i. According to the number and type of one-dimensional shape functions the resulting three-dimensional shape functions can be categorized into four groups of modes: *nodal modes*, *edge modes face modes* and *internal modes*. Figure 4 illustrates selected shape functions corresponding to the different classes for various polynomial degrees.

This mode of generating shape functions for brick-type elements allows for the choice of different approximation degrees in the different element directions. Spatially anisotropic approximations of the field variables are useful if 3D elements are used for lower dimensional structures such as shells, plates or beams. In these cases the degree of the in-plane approximation of the displacement field can be chosen arbitrarily high, whereas a quadratic or cubic approximation in thickness direction would be sufficient (Becker, Kuhl, and Meschke (2005)). Furthermore, this concept allows for a natural adaption of fieldwise approximations in multifield analyses to the specific requirements of the individual field variables (Becker, Jox, and Meschke (2009)).

4   Extension to coupled hygro-mechanical analyses

The extension to the hygro-mechanical model is formulated in the framework of the Theory of Porous Media (TPM) (see, e.g. Coussy (1989); Schrefler (1995); Ehlers and Bluhm (2000)). Full coupling between moisture transport and the mechanical behaviour of concrete are taken into account. Details of the formulation are contained in Grasberger and Meschke (2004); Meschke and Grasberger (2003) and, in the context of a higher order *p*-FEM formulation, in Becker, Jox, and Meschke (2009).
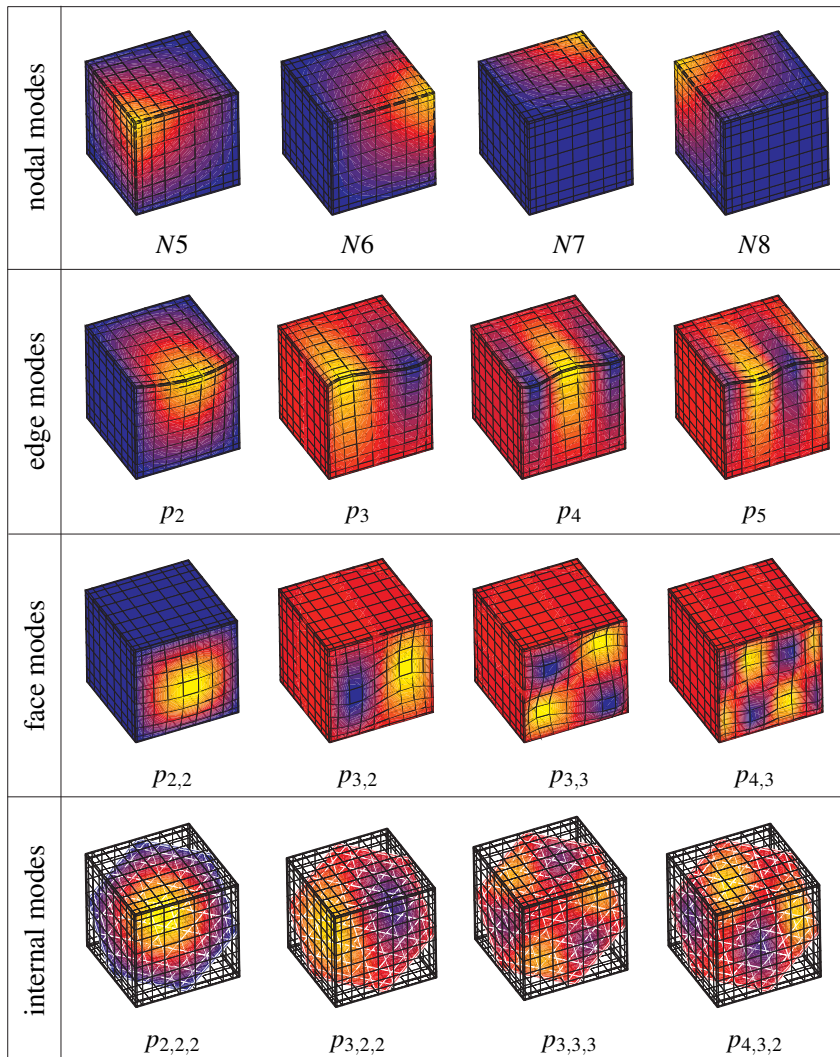
Figure 4: 3D-higher order shape functions: nodal, edge, face and internal modes for various polynomial degrees

The macroscopic capillary-pressure $p_c = p_g - p_l$, with the gaseous pressure p_g assumed to be equal to the atmospheric pressure taken as zero $p_g = 0$ and p_l as the liquid pressure, is considered as the basic variable for moisture transfer (Bear and Bachmat (1991)).
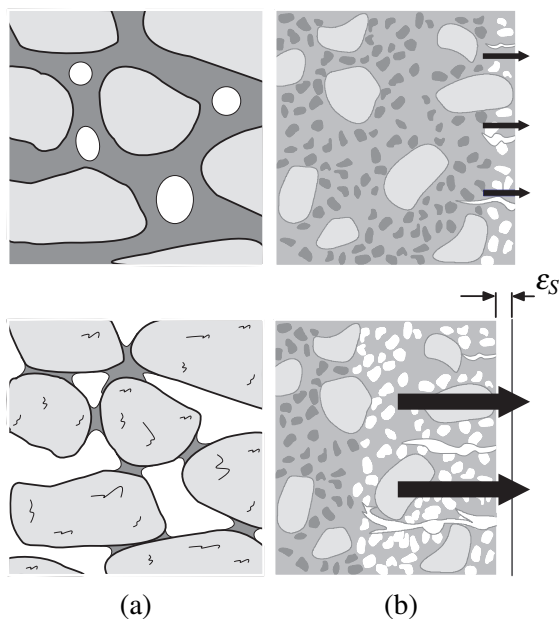

(a)   (b)

Figure 5: Effects of changing moisture conditions in cementitous materials: (a) Drying induces capillary forces; (b) Cracks promote transport of moisture

In cementitious materials such as concrete, saturation-dependent internal stresses develop as a consequence of molecular adsorption and capillary condensation. When subjected to drying, the internal stresses may lead to severe cracking in concrete structures when the material strength is exhausted. In turn, cracks strongly affect the permeability of the material (Figure 5). Details of the identification of the coupling coefficients are contained in Grasberger and Meschke (2004). Based upon the pore network model of Mualem (1976), the following relation between the capillary pressure and the liquid saturation as proposed by van Genuchten (1980)

$$S_l(p_c) = \left[1 + (p_c/p_r)^{\frac{1}{1-m}}\right]^{-m} \quad \text{for} \quad p_c > 0. \tag{19}$$

with the reference pressure $p_r = 18.6237\,N/mm^2$ and the coefficient $m = 0.4396$ specified in Baroghel-Bouny, Mainguy, Lassabatère, and Coussy (1999) for concrete, is used. The total stresses $\pm\sigma$ are expressed as a function of the effective

skeleton stresses $\pm\sigma'$, the BIOT coefficient b and the capillary pressure p_c

$$\pm\sigma = \pm\sigma' + bp_c\mathbf{1}. \tag{20}$$

The transport properties of concrete are strongly depending on the microstructure and the degree of cracking. In the proposed 3D model flow of moisture within the intact material is described by a DARCY model characterized by the (in general nonlinear) relation between the moisture flux $\mathbf{q}_l$ and the spatial gradient of the liquid pressure $\pm\nabla p$

$$\mathbf{q}_l = \frac{\rho_l}{\mu_l}\mathbf{k}_f(S_l)k_\phi(\phi) \pm \nabla p_c, \tag{21}$$

with the liquid permeability matrix $\mathbf{k}_f$, the dynamic viscosity μ_l of the liquid, the porosity ϕ and the mass density ρ_l. The permeability of the uncracked matrix material

$$\mathbf{k}_f(S_l) = k_r(S_l)\mathbf{k}_0 \tag{22}$$

with the intrinsic permeability $\mathbf{k}_0$ and the relative permeability $k_r(S_l)$ is formulated according to van Genuchten (1980) as

$$k_r(S_l) = \sqrt{S_l}\left[1 - (1 - S_l^{1/m})^m\right]^2 \tag{23}$$

with $0 < m < 1$.

The moisture flux along one single crack is modeled taking the solution of the NAVIER-STOKES equation for plane POISEUILLE flow with an idealized crack formation, assumed to be planar, parallel and of constant opening width w_c, as a starting point:

$$q_l^t = \frac{w_c^2}{12\,\mu_l}\nabla p_c. \tag{24}$$

Following the approach of Barton, Bandis, and Bakhtar (1985), taking into account the roughness of the cracks as well as the aperture variation and the tortuosity, the nominal crack width w_c is replaced by the equivalent hydraulic crack width

$$w_h = \frac{w_c^2}{R^{2.5}} \quad \text{for} \quad w_c \geq w_h \tag{25}$$

where the parameter R describes the roughness of the crack. This parameter has been determined in Meschke and Grasberger (2003) by means of reanalyses of two different series of tests performed by Aldea, Ghandehari, Shah, and Karr (2000);
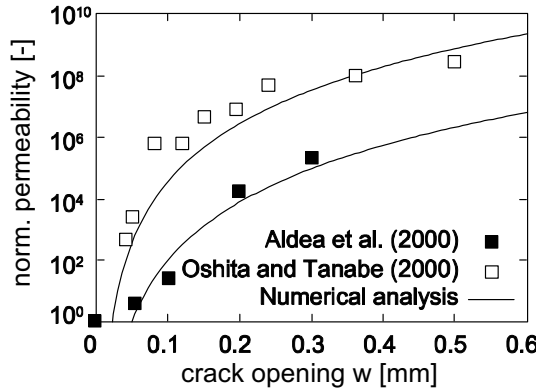
Figure 6: Moisture transport in cracks: Comparison between experimental and model results (Grasberger and Meschke (2004))

Oshita and Tanabe (2000). Accordingly, the permeability for cracks filled with water is expressed considering tortuosity effects along the crack channel Ω_S (see Figure 10) (Snow (1969)):

$$k_{c0}^{t}(w_h) = \frac{w_h^2}{12}. \tag{26}$$

The permeability of the evolving crack channel for partially filled cracks

$$k_c^t(S_l, w_h) = k_{rc}(S_l)k_{c0}^t(w_h) \tag{27}$$

depends on $k_{c0}^t(w_h)$ and the relative crack permeability

$$k_{rc}(S_l) = 8 \cdot 10^{-6} \exp(11.7S_l). \tag{28}$$

In a 3D setting the crack permeability in global coordinates is obtained from the transformation of the local permeability along the crack plane

$$\mathbf{k}_c^t = \begin{bmatrix} 0 & 0 & 0 \\ 0 & k_c(w_h, S_l) & 0 \\ 0 & 0 & k_c(w_h, S_l) \end{bmatrix} \tag{29}$$

using the transformation matrix $\mathbf{T}_c$ as

$$\mathbf{k}_c = \mathbf{T}_c^T \mathbf{k}_c^t \mathbf{T}_c. \tag{30}$$

5 Computational aspcets

For the incorporation of the *X*-FEM into the higher order *p*-FEM platform in a three-dimensional setting the following assumptions are made:

- Cracks are assumed to fully propagate through elements after the opening of a crack is signaled in the respective element. Hence, no crack-tip functions are used and the crack tip is represented by homogeneous boundary conditions for the enhanced displacement field at the crack front.

- Cracks are approximated as element-wise plane surfaces in the isoparametric domain. Consequently, in physical coordinates, non-plane surfaces according to the JACOBI-transformation are generated.

- An average weighted principal stress criterion characterized by the evaluation of the stresses within the integration points of the elements adjacent to the existing crack front and taking the principal values and axes of the averaged tensor is used to determine crack propagation and direction.

- The enhanced displacement field is restricted to linear approximations whereas the regular part is approximated arbitrarily high taking into account the kinematics associated with the specific geometry of the investigated structure, e.g. shell-like or slab-like structures:

$$\mathbf{u}(\mathbf{X}) \approx \sum_{i=1}^{NN_p} \mathbf{N}_{p1,p2,p3}\bar{\mathbf{u}}^{ei} + \sum_{j=1}^{8} \mathbf{N}_{1,1,1}S(\mathbf{X})\,\tilde{\mathbf{u}}^{ej}. \tag{31}$$

The hierarchical higher-order *p*-finite element formulation has proven its particular suitability in the context of coupled problems (see e.g Kuhl, Bangert, and Meschke (2004); Becker, Jox, and Meschke (2009)) which results from its ability to represent arbitrary complex (smooth) distributions of field variables by means of field-specific higher order shape functions. The combination of the extended (discontinuous) approximations according to the *X*-FEM for the representation of discontinuous distributions with higher-order *p* shape functions for the representation of smooth distributions of the field variables allows to simulate crack propagation in conjunction with multifield models without the need for mesh adaption using relatively coarse discretizations. Although higher-order polynomials for the regular and the enhanced displacement field are proposed in Moës, Dolbow, and Belytschko (1999), we follow the approach proposed by Stazi, Budyn, Chessa, and Belytschko (2003); Legay, Wang, and Belytschko (2005); Englund (2007), where different polynomial orders are used for both fields. Besides a reduction of numerical effort, linear dependencies of the enhanced shape functions with the standard

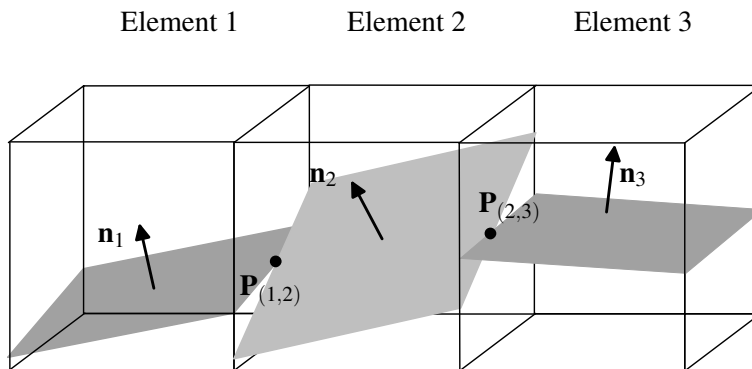Element 1   Element 2   Element 3

Figure 7: 3D crack tracking algorithm using 3D quadrilateral finite elements

higher order shape functions are a priori eliminated. It should be emphasized, that the investigation of interactions between the degree of approximation of the regular and the enhanced part of the displacement field was not within the focus of this paper. However, it should be noted, that, according to Laborde, Pommier, Renard, and Salaün (2005), optimal convergence is obtained if the same order of polynomial degree is used for the regular and the enhanced part of the displacement field. As was shown by Peters and Hackl (2009), using hierarchical higher order approximations for both the enhanced and the regular part together with crack tip functions also leads to an improved kinematics of the crack opening configuration.

5.1 *Crack tracking algorithm*

The representation of cracks as plane surfaces fully penetrating through finite elements requires special considerations as far as tracking of cracks is concerned. If a strictly C_0-continuous evolution of cracks would be followed (see e.g. Areias and Belytschko (2005)), in case that two intersections of an existing crack front with an uncracked element exist, the topology of the new crack plane opening in the uncracked element would be already defined by the two lines characterizing the two crack fronts, without taking into account any information regarding the direction of the new evolving crack from the cracking criterion. Therefore, a less strict algorithm is adopted, following suggestions made by Gasser and Holzapfel (2005). All element faces or facettes cut by the crack are considered as part of the crack front. Consequently, all elements that are not cut so far but include the crack front will be considered as potential cracking candidates. A crack plane is uniquely
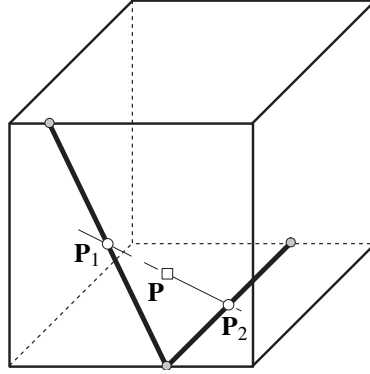
Figure 8: 3D crack tracking algorithm using 3D quadrilateral finite elements: Generation of the point **P** containing the new crack surface

defined by a point *P* of the potential new crack segment and the corresponding normal vector **n** established by the adopted principal stress criterion. **n** is the principal direction related to the maximum principal stress of the averaged stress tensor evaluated in the candidate element (Figure 7). Since the crack is assumed to propagate element-wise, the crack propagation criterion and the crack propagation direction are computed from average stresses instead from the local stress state at the crack front. In the proposed 3D implementation, the principal values and directions of the averaged stress tensor evaluated in the candidate element

$$\sigma = \frac{1}{\text{NGauss}} \sum_{m=1}^{\text{NGauss}} (\sigma_{ij} \, \mathbf{e}_i \otimes \mathbf{e}_j)_m \tag{32}$$

are computed. The largest principal value is taken for the check of crack propagation according to the RANKINE crack propagation criterion and the corresponding principal direction serves as the normal of the new crack segment. With this normal vector **n** and a point **P** defined according to the position of the current crack front(s), the position of the new crack surface is fully defined.

The position of the point *P* of the potential new crack segment is obtained as the vectorial average of the midpoints of all crack fronts connected with the considered candidate element (Figure 8):

$$\mathbf{P} = \sum_{i=1}^{n} \frac{\mathbf{P}_i}{n} \tag{33}$$

5.2 Visualization of the crack topology

Although the geometry of the crack surface is stored explicitly, for the visualization of the crack surface an implicit approach using the ϕ-level set method (Osher and Sethian, 1988; Osher and Fedkiw, 2003) is adopted. According to this method, the shortest distance of a particular point of the finite element with respect to the crack surface is represented by

$$\phi(\mathbf{X}) = [\mathbf{X} - \mathbf{X}_S] \cdot \mathbf{n} \quad \mathbf{X}_S \in \partial_S \Omega, \tag{34}$$

with $\mathbf{X}_S$ denoting a point on the crack surface $\partial_S \Omega$. The crack is visualized by plotting the $\phi = 0$ level set as an iso-surface.

5.3 Numerical Solution

In the context of a two-field hygro-mechanical model the primary variables $\mathbf{u}(\mathbf{x},t)$ and $p_c(\mathbf{x},t)$ in the domain Ω are governed by the balance of linear momentum and balance of liquid mass as

$$\text{div} \pm \sigma = 0, \quad \text{div}(\rho_l \mathbf{q}_l) + \dot{m} = 0. \tag{35}$$

In Eq.(35) body forces are neglected. The system of governing equations (35) is completed by the boundary conditions

$$\begin{aligned}
\pm\sigma(\mathbf{x},t) \cdot \mathbf{n}_\Gamma &= \mathbf{t}^*(t) \quad \forall \mathbf{x} \in \Gamma_\sigma, \quad \mathbf{q}_l(\mathbf{x},t) \cdot \mathbf{n}_\Gamma = q_l^*(t) \quad \forall \mathbf{x} \in \Gamma_{q_l}, \\
\mathbf{u}(\mathbf{x},t) &= \mathbf{u}^*(t) \quad \forall \mathbf{x} \in \Gamma_u, \quad p_c(\mathbf{x},t) = p_c^*(t) \qquad \forall \mathbf{x} \in \Gamma_{p_c}
\end{aligned} \tag{36}$$

and the initial conditions

$$\mathbf{u}(\mathbf{x}, t = 0) = \mathbf{u}_0, \quad p_c(t = 0) = p_{c,0}. \tag{37}$$

$\mathbf{n}_\Gamma$ is the normal vector on the boundary of the structure, q_l^* is the liquid flux across the boundary, p_c^* is the prescribed capillary pressure, $\mathbf{u}^*$ is the prescribed displacement and $\mathbf{t}^*$ the traction vector on the boundary.

The weak form of the balance of momentum is obtained according to Eq.(7) after inserting Eq.(20) as

$$\begin{aligned}
\delta W_m &= \int_{\Omega^e} \delta \pm\varepsilon : \pm\sigma \, dV - \int_{\Gamma_\sigma} \delta \mathbf{u} \cdot \mathbf{t}^* \, dA \\
&= \int_{\Omega^e} \nabla \delta \bar{\mathbf{u}} : \left(\pm\sigma' + b p_c \mathbf{1} \right) dV + \int_{\Omega^{+-}} S_S \nabla \delta \hat{\mathbf{u}} : \left(\pm\sigma' + b p_c \mathbf{1} \right) dV \\
&\quad + 2 \int_{\partial_S \Omega^e} \delta \hat{\mathbf{u}} \cdot \underbrace{\left(\mathbf{t}'_S + b p_c \mathbf{n}_S \right)}_{\mathbf{t}_S} dA - \int_{\Gamma_\sigma} \delta \mathbf{u} \cdot \mathbf{t}^* \, dA,
\end{aligned} \tag{38}$$

with the total and effective traction vectors $(\mathbf{t}_S(\llbracket \mathbf{u} \rrbracket, p_c))$ and $(\mathbf{t}'_S(\llbracket \mathbf{u} \rrbracket))$ at the surface of discontinuity $\partial_S \Omega^e$. The weak form of balance of liquid mass and the hygral NEUMANN boundary conditions reads

$$\delta W_h = \int_{\Omega^e} \delta p_c \frac{\dot{m}_l}{\rho_l} \, dV - \int_{\Omega^e} \delta \pm \nabla p_c \cdot \mathbf{q}_l \, dV - \int_{\Gamma_q} \delta p_c \, q_l^* \, dA = 0. \tag{39}$$

Spatial discretization of Eqs.(38) and (39) yields the semi-discrete coupled set of equations

$$\mathbf{S}^e(\mathbf{x}^e) \dot{\mathbf{x}}^e + \mathbf{K}^e(\mathbf{x}^e) \mathbf{x}^e = \mathbf{r}^e(\mathbf{x}^e) \tag{40}$$

with the storage and stiffness matrices

$$\mathbf{S}^e = \begin{bmatrix} \mathbf{0} & \mathbf{0} & \mathbf{0} \\ \mathbf{0} & \mathbf{0} & \mathbf{0} \\ \mathbf{Q}_{p\bar{u}} & \mathbf{Q}_{p\hat{u}} & \mathbf{S}_{pp} \end{bmatrix}, \quad \mathbf{K}^e = \begin{bmatrix} \mathbf{K}_{\bar{u}\bar{u}} & \mathbf{K}_{\bar{u}\hat{u}} & \mathbf{Q}_{\bar{u}p} \\ \mathbf{K}_{\hat{u}\bar{u}} & \mathbf{K}_{\hat{u}\hat{u}} & \mathbf{Q}_{\hat{u}p} \\ \mathbf{0} & \mathbf{0} & \mathbf{H}_{pp} \end{bmatrix} \tag{41}$$

and the nodal degrees of freedom and nodal forces

$$\dot{\mathbf{x}}^e = \begin{bmatrix} \dot{\bar{\mathbf{u}}} \\ \dot{\hat{\mathbf{u}}} \\ \dot{\mathbf{p}}_c \end{bmatrix} \quad \mathbf{x}^e = \begin{bmatrix} \bar{\mathbf{u}} \\ \hat{\mathbf{u}} \\ \mathbf{p} \end{bmatrix} \quad \mathbf{r}^e = \begin{bmatrix} \mathbf{r}_{\bar{u}} \\ \mathbf{r}_{\hat{u}} \\ \mathbf{r}_p \end{bmatrix}. \tag{42}$$

After assembly, applying time discretization using finite differences together with a fully implicit time integration scheme and consistent linearization by means of the NEWTON-RAPHSON algorithm (Lewis and Schrefler (1998)) the resulting algebraic system of equations is solved within the time interval $[t_n, t_{n+1}]$:

$$[\mathbf{S} + \Delta t \, \mathbf{K}]_{n+1} \, \mathbf{x}_{n+1} = \mathbf{S} \, \mathbf{x}_n + \Delta t \, \mathbf{r}_{n+1}. \tag{43}$$

5.4 Numerical integration

For the numerical integration of the weak form (38) and (39) at the element level the discontinuous character of the enhanced strain field has to be taken into account. Consequently, both parts of elements separated by a crack plane have to be integrated separately. As a more efficient alternative to a standard subdivision using DELAUNEY-triangularization, cracked elements are subdivided into a fixed set of six sub-tetrahedrons (Figure 9). For each of these tetrahedrons it is checked, whether it contains the crack plane segment. The crack plane cutting the element may either have a triangular or a quadrilateral shape. Consequently, a sub-tetrahedron can be split into two tetrahedrons, two pentahedrons, a tetrahedron
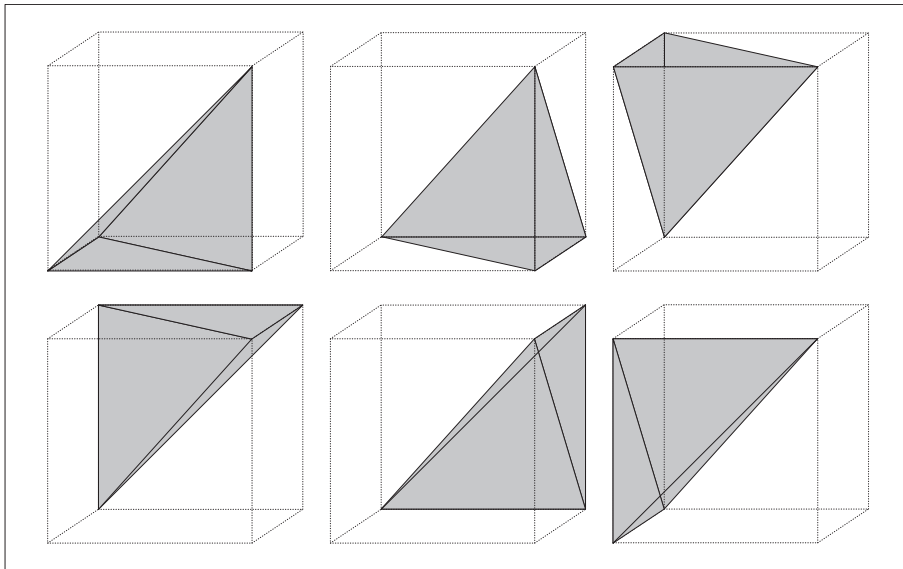
Figure 9: Numerical intgeration of cracked elements: Subdivision of the element into six sub-tetrahedrons

and a pentahedron or into a tetrahedron and a pyramid. For the integration of the traction-separation law and the moisture flow the respective subdomains are either triangles or quadrilaterals. The volume integral of a cracked finite element is computed, after transformation to natural element coordinates ξ^i with the help of the Jacobian $\mathbf{J}$, by summing all contributions of *nsub* sub-continua that are integrated numerically over the natural coordinates η^j of the sub-domains:

$$\int_{\Omega^e} (\bullet) \, dV = \int_{V_\xi} (\bullet) \underbrace{||\frac{\partial \mathbf{X}}{\partial \pm \xi}||}_{||\mathbf{J}||} dV_\xi = \sum_{i=1}^{nsub} \int_{V_\eta} (\bullet) ||\frac{\partial \mathbf{X}}{\partial \pm \xi} \frac{\partial \pm \xi}{\partial \pm \eta}|| dV_\eta. \tag{44}$$

The relation between both natural coordinates $\pm \xi = \pm \xi(\pm \eta)$ is obtained from determining the ξ^i coordinates of the nodes of the sub-domains. These correspond either to the vertices of the element or to points on the crack surface. The latter ones are identified with the help of the ϕ-level sets.

5.5 Numerical integration of the crack channel

Intact parts and the crack plane have to be considered as different domains in the integration procedure. Hence, the stiffness matrix $\mathbf{K}_{\hat{u}\hat{u}}$ and the liquid permeability
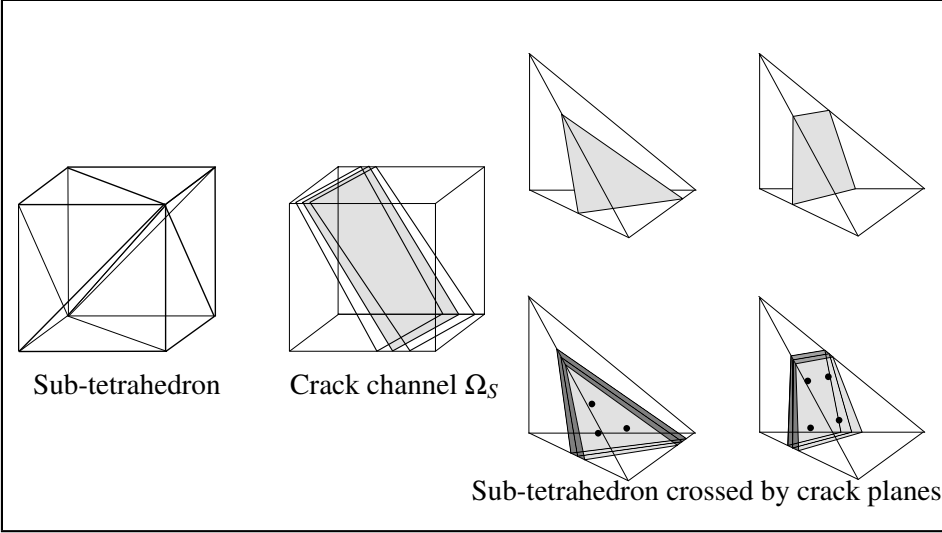
Figure 10: Integration concept: Separate integration of sub-continua (sub-tetahedrons) and the crack channel Ω_S

matrix $\mathbf{H}_{pp}$ are evaluated as

$$
\begin{aligned}
\mathbf{K}_{\hat{u}\hat{u}} &= \int\limits_{\Omega^{+-}} S_S^2 \mathbf{B}_u^T \mathbf{C} \mathbf{B}_u \, dV + \int\limits_{\partial_S\Omega} \mathbf{N}_u^T \mathbf{T} \mathbf{N}_u \, dA, \\
\mathbf{H}_{pp} &= -\int\limits_{\Omega} \mathbf{B}_p^T \mathbf{k}_f / \mu_l \, \mathbf{B}_p \, dV - \int\limits_{\Omega_S} \mathbf{B}_p^T \mathbf{A}^T \, k_c^t(w)/\mu_l \, \mathbf{A} \mathbf{B}_p \, dV.
\end{aligned}
\tag{45}
$$

$\mathbf{N}_u$ contains the hierarchical shape functions of the displacement field, $\mathbf{B}_u$ and $\mathbf{B}_p$ are the gradient matrices of the displacement and the capillary pressure field and $k_c^t(w)$ is the liquid permeability in the crack channel according to Eq.(29). The matrix $\mathbf{A}(\mathbf{n})$ is the projection of ∇p_c onto the crack channel characterized by the normal unit vector $\mathbf{n}$.

The permeability matrix $\mathbf{H}_{pp}$ is computed as

$$
\mathbf{H}_{pp} \sim -\sum_{n=1}^{GP_p} \mathbf{B}_p^T \mathbf{k}_f / \mu_l \, \mathbf{B}_p |\mathbf{J}_n| \alpha_n - \sum_{j=1}^{GP_c} \mathbf{B}_p^T \mathbf{A}^T \, k_c^t(w)/\mu_l \, \mathbf{A} \mathbf{B}_p \, w_j |\mathbf{J}_{\partial_S\Omega,j}| \, \alpha_j,
\tag{46}
$$

using GP_p integration points for the continuum and GP_c integration points for the crack channel (Figure 10). The integration is performed either over triangles or quadrilaterals according to the integration concept described above.

6   Numerical examples

6.1   *Cracking of a double notched slab*

As a first benchmark example a double notched slab subjected to a combined loading of shear and normal forces which has been investigated experimentally by (Nooru-Mohamed, 1992) is analyzed using the proposed 3D *X*-FEM model. The geometry, material parameters and the finite element discretization are contained in Figure 11. According to the geometry of the slab the approximation of the dis-
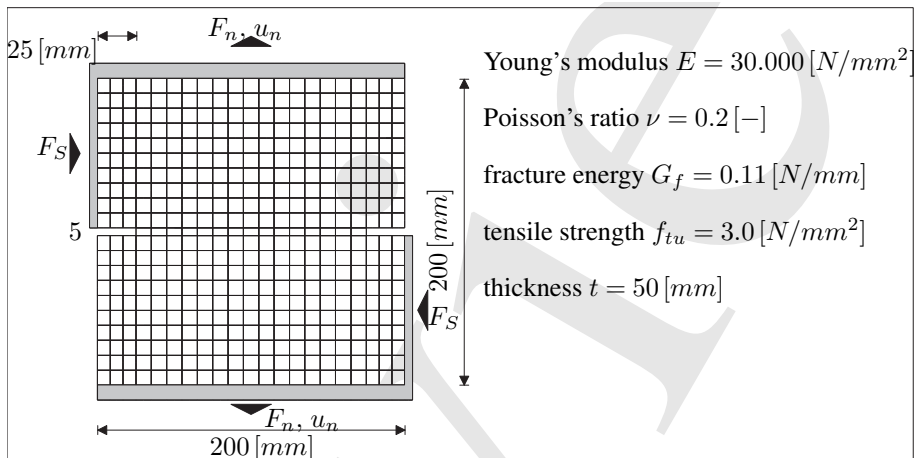

Figure 11: 3D *X*-FEM analysis of a double notched slab: geometry, material parameter and finite element mesh

placement field is chosen as $\mathbf{u} \approx \mathbf{u}_{3,3,1}$. In a first loading stage, the slab is subjected to a shear force $F_s = 10\,kN$. Subsequently, keeping the load level of the shear force constant, a normal force F_n is applied incrementally by controlling the respective displacement.

Figure 12 illustrates the curved crack paths obtained from the proposed crack model for the combined loading scenario. The visualization of the crack path is accomplished by plotting the $\phi = 0$-level set. The left hand side of Figure 13 shows a comparison of the crack topologies obtained from the present 3D *X*-FEM model using a *slab-like* higher order solid FEM formulation, with a variational 2D *X*-FEM model proposed by (Meschke and Dumstorff, 2007) and with the experimentally determined range of cracks (in grey color). The crack topology obtained from the proposed 3D *X*-FEM model correlates well with the experimental results and the results from 2D analyses using a variational *X*-FEM model with crack tip enhance-
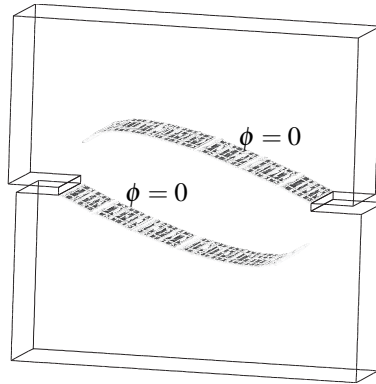
Figure 12: 3D *X*-FEM analysis of a double notched slab: Visualization of the crack topology by the $\phi = 0$-level set
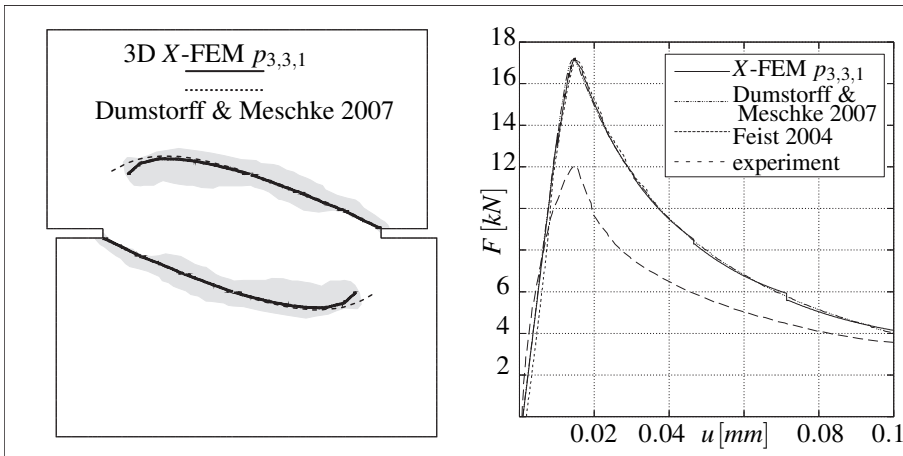

Figure 13: 3D *X*-FEM analysis of a double notched slab: Comparisons of results from the proposed 3D *X*-FEM model with a variational 2D *X*-FEM model (Meschke and Dumstorff, 2007) and the experimental results. left: crack topologies, right: load-displacement curves

ments (Meschke and Dumstorff, 2007). Figure 13 (right) shows a comparison of the corresponding load displacement curves. In this figure, also computational results from (Feist, 2004) are included. All three numerical results are within a relativley small range while they differ significantly with respect to the experimental results.

It should be emphasized, that, due to the lack of reported material parameters the set of parameters taken by (Feist, 2004; Meschke and Dumstorff, 2007) has been adopted.

6.2   Anchor pull-out test

To illustrate the capability of the proposed three-dimensional implementation of the Extended Finite Element Method in a fully 3D situation, an anchor pull-out test is investigated numerically. Figure14 shows the analyzed structure and the corresponding finite element mesh using 996 elements. The material parameters are
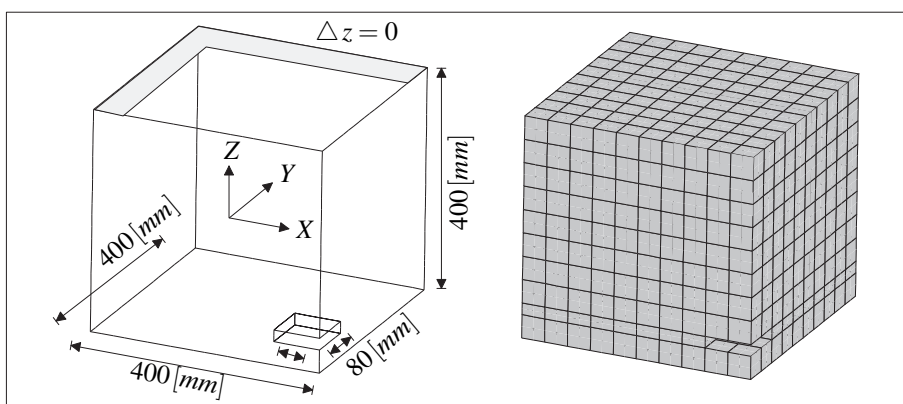

Figure 14: Numerical analysis of an anchor pull-out test: Geometry and finite element mesh ($NE = 996$)

the same as used previously for the numerical analysis of the double-notched slab. Due to symmetry only one quarter of the structure is discretized. The pull-out of the anchor is simulated by applying displacements on the bottom side of the elements representing the counterpart of the anchor plates. The anchor itself is not discretized. The displacements are approximated by tri-quadratic shape functions ($\mathbf{u} = \mathbf{u}_{2,2,2}$). Along the shaded part of the top surface (Figure14) the concrete specimen is supported in z-direction. Figure 15 (left) shows the resulting crack surface of the pull-out test. This figure illustrates the three-dimensional character of the crack surface and its conical propagation from the anchor plate towards the supporting area at the top face of the specimen. It is observed that the gaps between crack surface segments resulting from the C_0-discontinuous crack tracking algorithm are marginal. Figure 15 (right) illustrates the displacement component u_z in pull-out direction. The jump of the displacement component u_z at the position of the determined crack surface indicates a complete separation of the upper and lower part
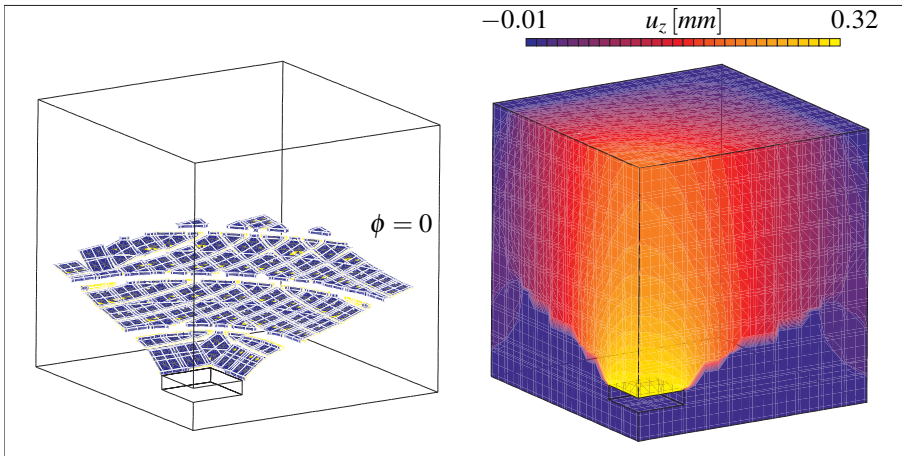
Figure 15: Numerical analysis of an anchor pull-out test: left: crack topology, right: distribution of displacement u_3 in pull-out direction
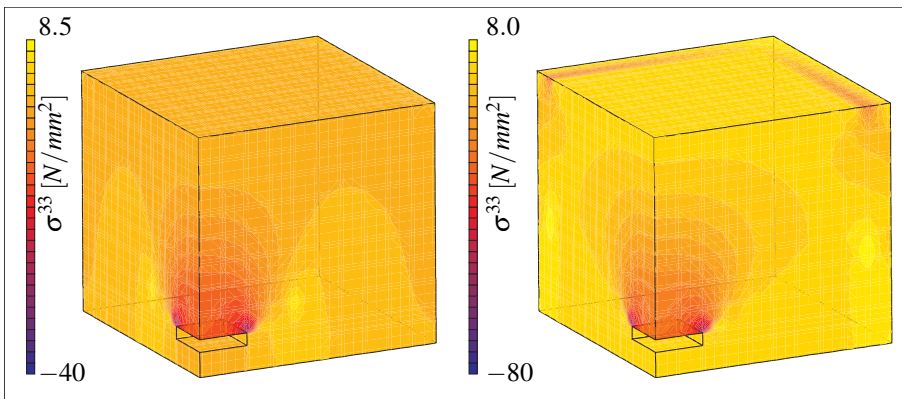

Figure 16: Numerical analysis of an anchor pull-out test: left: stress component σ^{33} at an initial stage of the pull-out process, right: stress component σ^{33} at the end of crack process

of the concrete structure. Figure 17 contains the load displacement curve obtained from the numerical analysis. The irregularities in this curve reflect the cracking of single elements resulting from the elementwise crack propagation algorithm.

In an initial stage, the curve shows a linear elastic behavior of the structure up to a prescribed displacement of $u_z \approx 0.04\,mm$. Subsequently, a nonlinear relation be-
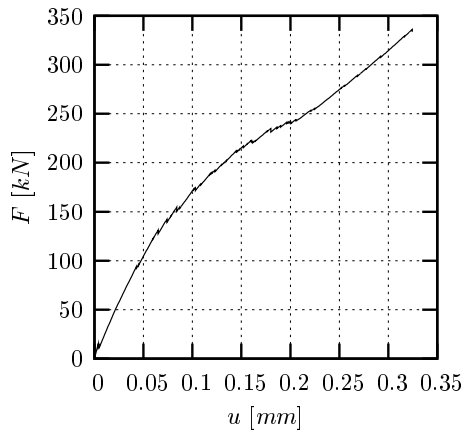
Figure 17: Numerical analysis of an anchor pull-out test: load-displacement curve

tween the applied load and the displacement of the anchor plate is observed, without, however, showing a structural softening behavior. During this phase, a crack surface emanates from the anchor plate with a relatively small inclination which prevents the crack surface reaching the top surface and therefore prevents structural softening. Hence, after the displacement has reached a level of $u_z \approx 0.21\,mm$, the response of the structure is again more or less linear since the crack evolution comes to a standstill and the stresses are transferred directly to the supporting area at the top surface.

This observed structural behavior is a consequence of the fact, that, due to the specific geometry of the chosen example, the fracture cone does not fully penetrate up to the top surface and the load is transferred via inclined compressive struts. If the present model for mode I fracture would be supplemented by a comprehensive 3D model for concrete which also accounts for failure in compression and shear, structural softening would also be observed for the present example (Gasser and Holzapfel (2005)).

Figure 16 illustrates the distribution of the stress component σ^{33} in two loading stages. Figure16 (right) shows the strongly increased level of the stress component σ^{33} along the supporting area after the cracking process has come to an end compared to the initial stage (Figure16 left).

6.3   *Drying of a three-point bending beam*

The applicability of the proposed finite element formulation for prognoses of moisture transport in cracks is shown by the numerical analysis of a notched three point
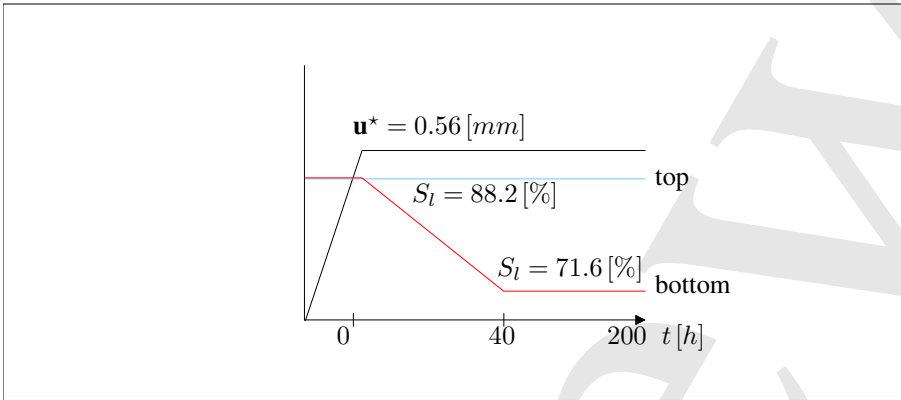
Figure 18: Hygro-mechanical simulation of a concrete beam: geometry, material parameters and finite element mesh
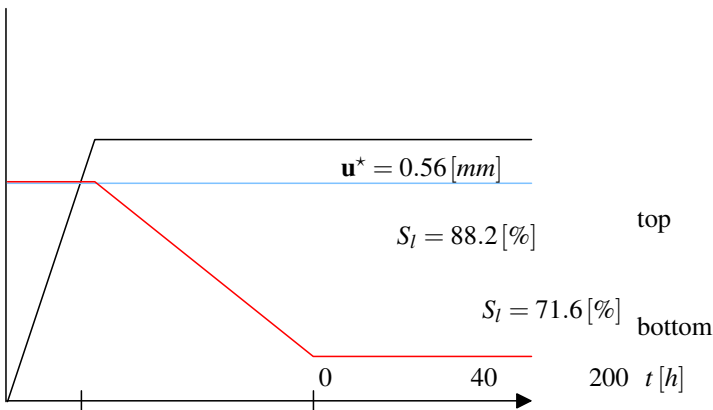

Figure 19: Hygro-mechanical simulation of a concrete beam: mechanical and hygral loading history

bending beam subjected to drying. Figure 18 contains the geometry, the mechanical and hygral boundary conditions, the material parameters and the spatial discretization by means of 272 3D-p-elements. For the approximation of the regular displacement field, the anisotropic Ansatz $\mathbf{u} \approx \mathbf{u}_{2,2,1}$ is chosen while trilinear shape functions are used for the enhanced displacements and the capillary pressure, respectively. Figure 19 illustrates the mechanical and hygral loading history of the beam structure. A fixed crack located in the center at the bottom side of the beam with a length of $3.25\,mm$ is generated by applying a displacement $u^* = 0.56\,mm$

at the center of the top face of the beam. After applying the mechanical loading a drying process at the lower face, starting from a liquid saturation of $S_l^* = 88.2\%$ ($p_c = 10.0\,N/mm^2$) to a final saturation of $S_l^* = 58.8\%$ ($p_c = 20.0\,N/mm^2$) is prescribed while the liquid saturation at the upper face remains constant. Due to the drying process, the existing crack opens (Figure 20).
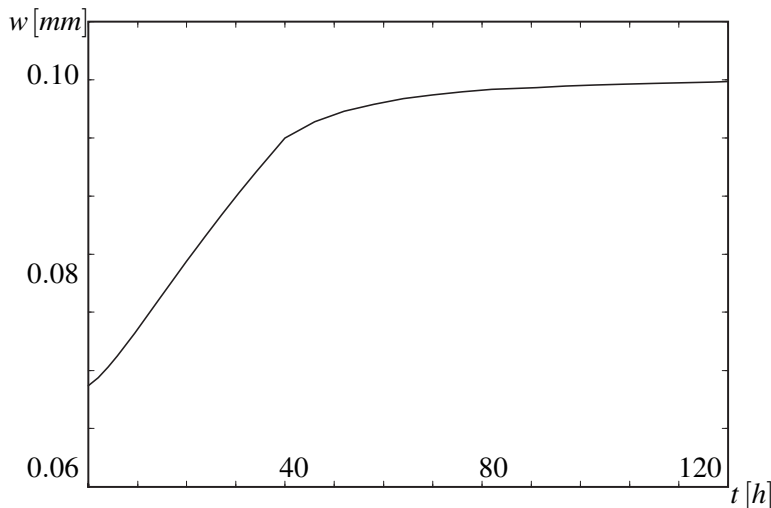

Figure 20: Hygro-mechanical simulation of a concrete beam: temporal evolution of the crack opening

Figure 21 illustrates the distribution of capillary pressure p_c in the vicinity of the crack at different stages of the drying process. Due to the hygral environmental conditions, the moisture front penetrates from the bottom upwards. In the vicinity of the crack, an accelerated drying process is observed. This is also illustrated on the left hand side of Figure 21 showing the distribution of the capillary pressure p_c along the height of the beam at the position of the initial crack at different stages of the drying process.

7   Conclusions

A three-dimensional implementation of the Extended Finite Element Method (X-FEM) for the numerical analysis of cohesive cracks in cementitious materials, such as concrete, was presented in a hygro-mechanical modeling framework in conjunction with a p-finite element (p-FEM) strategy based on hierarchical higher order shape functions has been presented. The hygro-mechanical model for partially saturated cementitious materials is based upon the Theory of Porous Media and allows for the representations of relevant hygro-mechanical couplings within the
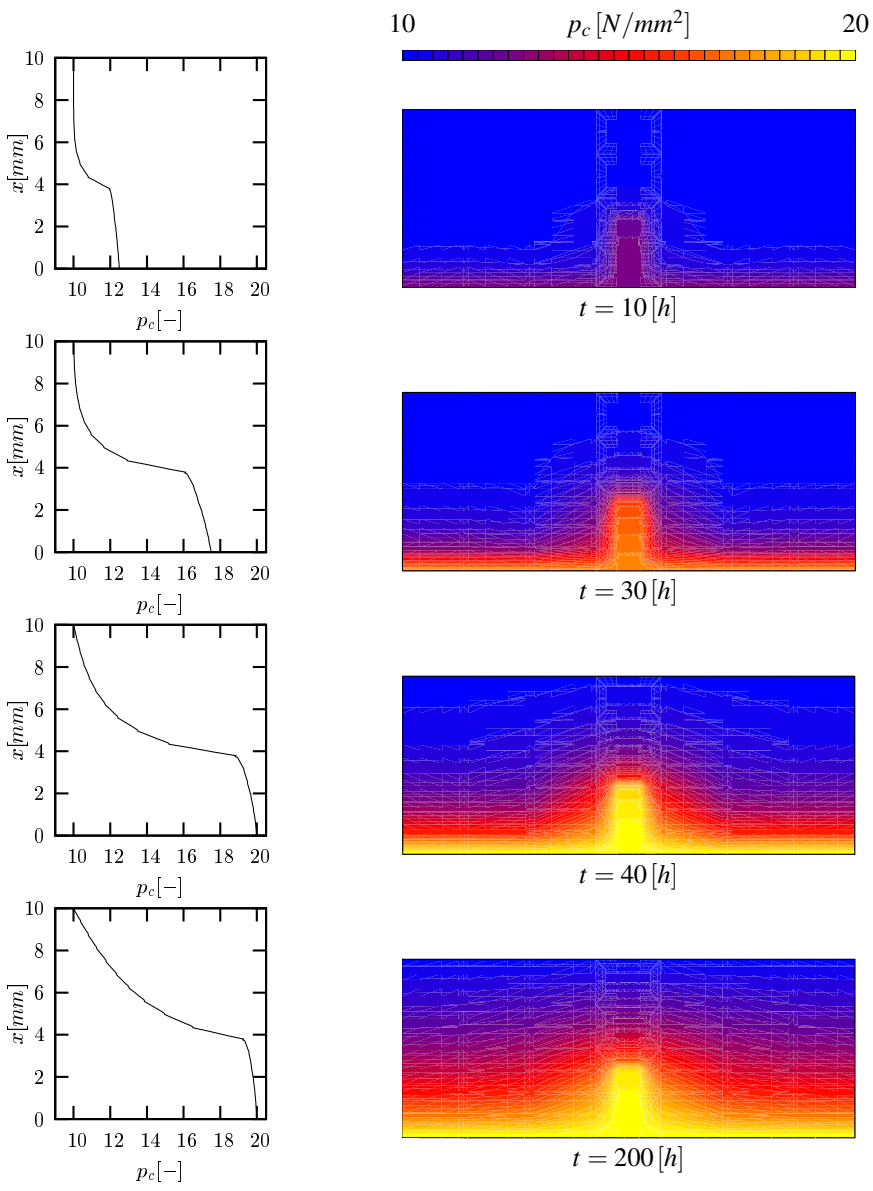
Figure 21: Hygro-mechanical simulation of a concrete beam: temporal evolution of the capillary pressure in the vicinity of the initial crack

intact parts of the material. The *X*-FEM implementation is characterized by an efficient integration scheme using pre-defined subdomains and crack tracking algorithms allowing for discontinuities between adjacent crack surfaces in neighboring elements. The *p*-FEM modeling platform allows for anisotropic, field-specific higher order approximations considering the specific requirements associated with the geometry of the structure and the individual field variables. Interactions between evolving cracks and the accelerated moisture transport has been taken into account by means of a POISEUILLE flow model together with a separate integration along the crack channel. The performance of the proposed 3D higher order *X*-FEM model has been demonstrated by two crack propagation analyses and one hygro-mechanical analysis of a concrete beam. The re-analyses of a double-notched concrete slab has shown a good agreement with 2D analyses published previously as well as with experimental results. In the analysis of a pullout test it was shown that a more or less smooth crack surface resulting from the pullout of an anchor from a concrete specimen is generated by the adopted discontinuous crack tracking algorithm. From the hygro-mechanical analysis of the drying of a pre-cracked concrete beam the capability of the coupled model to represent the accelerated transport of moisture through the crack channel has been demonstrated.

References

Aldea, C.-M.; Ghandehari, M.; Shah, S.; Karr, A. (2000): Estimation of water flow through cracked concrete under load. *ACI Materials Journal*, vol. 97, pp. 567–575.

Areias, P.; Belytschko, T. (2005): Analysis of three-dimensional crack initiation and propagation using the extended finite element method. *International Journal for Numerical Methods in Engineering*, vol. 63, pp. 760–788.

Armero, F.; Garikipati, K. (1996): An analysis of strong discontinuities in multiplicative finite strain plasticity and their relation with the numerical simulation of strain localization in solids. *International Journal of Solids and Structures*, vol. 33, no. 20, pp. 2863–2885.

Asferg, J.; Poulsen, P.; Nielsen, L. (2005): Cohesive crack tip element for X-FEM. In Carpinteri, A.(Ed): *International Conference on Fracture (ICF 11)*. CDROM.

Baroghel-Bouny, V.; Mainguy, M.; Lassabatère, T.; Coussy, O. (1999): Characterization and identification of equilibrium and transfer moisture properties for ordinary and high-performance cementitious materials. *Cement and Concrete Research*, vol. 29, pp. 1225–1238.

Barton, N.; Bandis, S.; Bakhtar, K. (1985): Strength, deformation and conductivity coupling of rock joints. *International Journal of Rock Mechanics and Mining Sciences & Geomechanics Abstracts*, vol. 22, pp. 121–140.

Bear, J.; Bachmat, Y. (1991): *Introduction to Modeling of Transport Phenomena in Porous Media*. Kluwer Academic Publisher, Dordrecht, The Netherlands.

Becker, C.; Jox, S.; Meschke, G. (2009): Anisotropic and field-specific higher order spatial discretization methods for multiphase durability analyses. *Computers & Structures*, vol. 87, pp. 1349–1359.

Becker, C.; Kuhl, D.; Meschke, G. (2005): Higher order discretization concepts for durability-oriented multifield analyses of structures. In Ramm, E.; Wall, W.; Bletzinger, K.-U.; Bischoff, M.(Eds): *5th International Conference on Computation of Shell and Spatial Structures*. CD-ROM.

Belytschko, T.; Möes, N.; Usui, S.; Parimi, C. (2001): Arbitrary discontinuities in finite elements. *International Journal for Numerical Methods in Engineering*, vol. 50, pp. 993–1013.

Camacho, G.; Ortiz, M. (1996): Computational modelling of impact damage in brittle materials. *International Journal for Solids and Structures*, vol. 33, pp. 2899–2938.

Coussy, O. (1989): Thermomechanics of saturated porous solids in finite deformation. *European Journal of Mechanics, A/Solids*, vol. 8, pp. 1–14.

Coussy, O.; Ulm, F.-J. (2001): Elements of durability mechanics of concrete structures. In F.-J. Ulm, Z. B.; Wittmann, F.(Eds): *Creep, Shrinkage and Durability Mechanics of Concrete and Other Quasi-Brittle Materials*, pp. 393–409, Amsterdam, Netherlands. Elsevier.

de Borst, R. (2002): Some recent issues in computational failure mechanics. *International Journal for Numerical Methods in Engineering*, vol. 52, pp. 63–95.

Dumstorff, P.; Meschke, G. (2007): Crack propagation criteria in the framework of X-FEM-based structural analyses. *International Journal for Numerical and Analytical Methods in Geomechanics*, vol. 31, pp. 239–259.

Dumstorff, P.; Mosler, J.; Meschke, G. (2003): Advanced discretization methods for cracked structures: The Strong Discontinuity approach vs. the Extended Finite Element Method. In *Computational Plasticity 2003*. CIMNE, Barcelona, CD-ROM.

Düster, A. (2002): *High order finite elements for three-dimensional, thin-walled nonlinear continua*. Shaker-Verlag, Aachen. Dissertation, Technische Universität München.

Ehlers, W.; Bluhm, J. (2000):   *Porous Media*. Springer.

Englund, J. (2007):   A higher order scheme for two-dimensional quasi-static crack growth simulations. *Comput. Methods Appl. Mech. Engrg.*, vol. 196.

Feist, C. (2004):   *A Numerical Model for Cracking of Plain Concrete Based on the Strong Discontinuity Approach*. PhD thesis, Institut für Baustatik, Festigkeitslehre und Tragwerkslehre, Universität Innsbruck, 2004.

Feist, C.; Hofstetter, G. (2006):   An embedded strong discontinuity model for cracking of plain concrete. *Computer Methods in Applied Mechanics and Engineering*, vol. 195, no. 52, pp. 7115–7138.

Gasser, T.; Holzapfel, G. (2005):   Modeling 3D crack propagation in unreinforced concrete using PUFEM. *Computer Methods in Applied Mechanics and Engineering*, vol. 194, pp. 2859–2896.

Grasberger, S.; Meschke, G. (2004):   Thermo-hygro-mechanical degradation of concrete: From coupled 3D material modelling to durability-oriented multifield structural analyses. *Materials and Structures*, vol. 37, pp. 244–256. Special Issue on Poromechanis of Concrete).

Gravouil, A.; Moës, N.; Belytschko, T. (2002):   Non-planar 3D crack growth by the extended finite element and level sets - Part II: Level set update. *International Journal for Numerical Methods in Engineering*, vol. 53, pp. 2569–2586.

Ingraffea, A.; Saouma, V. (1985):   Numerical modelling of discrete crack propagation in reinforced and plain concrete. In Sih, G.; DiTommaso, A.(Eds): *Fracture Mechanics of Concrete: structural application and numerical calculation*, pp. 171–225. Martinus Nijhoff.

J ager, P.; Steinmann, P.; Kuhl, E. (2008):   Modelling three-dimensional crack propagation. A comparison of crack path tracking strategies. *International Journal for Numerical Methods in Engineering*, vol. 76, no. 9, pp. 1328 – 1352.

Jirásek, M.; Belytschko, T. (2002):   Computational resolution of strong discontinuities. In Mang, H.; Rammerstorfer, F.; Eberhardsteiner, J.(Eds):   *Fifth World Congress on Computational Mechanics*, Vienna, Austria.

Jirásek, M.; Zimmermann, T. (2001):   Embedded crack model: Part 1: Basic formulation. part 2: Combination with smeared cracks. *International Journal for Numerical Methods in Engineering*, vol. 50, pp. 1269–1305.

Kuhl, D.; Bangert, F.; Meschke, G. (2004):   Coupled chemo-mechanical deterioration of cementitious materials. Part II: Numerical methods and simulations. *International Journal of Solids and Structures*, vol. 41, pp. 41–67.

Laborde, P.; Pommier, J.; Renard, Y.; Salaün, M. (2005): High-order extended finite element method for cracked domains. *Int. J. Numer. Methods Engng.*, vol. 64.

Legay, A.; Wang, H.; Belytschko, T. (2005): Strong and weak arbitrary discontinuities in spectral finite elements. *Int. J. Numer. Methods Engng.*, vol. 64.

Lewis, R.; Schrefler, B. (1998): *The Finite Element Method in the Static and Dynamic Deformation and Consolidation of Porous Media*. John Wiley & Sons, Chichester.

Maekawa, K.; Ishida, T. (2002): Modeling of structural performanaces under coupled environmental and weather actions. *Materials and Structures*, vol. 35, pp. 591–602.

Mang, H.; Meschke, G.; Lackner, R.; Mosler, J. (2003): *Comprehensive Structural Integrity*, volume 3, chapter Computational Modelling of concrete Structures, pp. 1–67. Elsevier, 2003.

Mariani, S.; Perego, U. (2003): Extended finite element method for quasi-brittle fractur. *International Journal for Numerical Methods in Engineering*, vol. 58, pp. 103–126.

Mergheim, J.; Kuhl, E.; Steinmann, P. (2005): A finite element method for the computational modelling of cohesive cracks. *International Journal for Numerical Methods in Engineering*, vol. 63, pp. 276–289.

Meschke, G.; Dumstorff, P. (2007): Energy-based modeling of cohesive and cohesionless cracks via X-FEM. *Computer Methods in Applied Mechanics and Engineering*, vol. 196, pp. 2338–2357.

Meschke, G.; Grasberger, S. (2003): Numerical modelling of coupled hygro-mechanical degradation of cementitious materials. *Journal of Engineering Mechanics (ASCE)*, vol. 129, no. 4, pp. 383–392.

Moës, N.; Belytschko, T. (2002): Extended finite element method for cohesive crack growth. *Engineering Fracture Mechanics*, vol. 69, pp. 813–833.

Moës, N.; Dolbow, J.; Belytschko, T. (1999): A finite element method for crack growth without remeshing. *International Journal for Numerical Methods in Engineering*, vol. 46, pp. 131–150.

Moës, N.; Gravouil, A.; Belytschko, T. (2002): Non-planar 3D crack growth by the extended finite element and level sets - Part I: Mechanical model. *International Journal for Numerical Methods in Engineering*, vol. 53, pp. 2549–2568.

Moës, N.; Sukumar, N.; Moran, B.; Belytschko, T. (2000): An extended finite element method (X-FEM) for two- and three-dimensional crack modeling. In *Eu-*

ropean Congress on Computational Methods in Applied Sciences and Engineering, Barcelona, Spain.

Mosler, J.; Meschke, G. (2003): 3D modeling of strong discontinuities in elasto-plastic solids: Fixed and rotating localization formulations. *International Journal for Numerical Methods in Engineering*, vol. 57, pp. 1553–1576.

Mualem, Y. (1976): A new model for predicting the hydraulic conductivity of unsaturated porous media. *Water Resources Research*, vol. 12, pp. 513–522.

Nooru-Mohamed, M. (1992): *Mixed-mode Fracture of Concrete: an Experimental Approach*. PhD thesis, Technische Universiteit Delft, 1992.

Oliver, J. (1996): Modelling strong discontinuities in solid mechanics via strain softening constitutive equations. Part 1: Fundamentals, Part 2: Numerical simulation. *International Journal for Numerical Methods in Engineering*, vol. 39, pp. 3575–3623.

Oliver, J.; Huespe, A. (2002): On strategies for tracking strong discontinuities in computational failure mechanics. In *Online Proceedings of the Fifth World Congress on Computational Mechanics (WCCM V)*.

Osher, S.; Fedkiw, R. (2003): *Level Set Methods and Dynamics Implicit Surfaces*. Springer, New York.

Osher, S.; Sethian, J. (1988): Fronts propagating with curvature depending speed: algorithms based on Hamilton-Jacobi formulations. *Journal of Computational Physics*, vol. 79, pp. 12–49.

Oshita, H.; Tanabe, T. (2000): Modeling of water migration phenomenon in concrete as homogeneous material. *Journal of Engineering Mechanics (ASCE)*, vol. 126, pp. 551–553.

Peters, M.; Hackl, K. (2009): p-version of the X-FEM. In Stangenberg, F.; Breitenbücher, R.; Bruhns, O.; Hartmann, D.; Höffer, R.; Kuhl, D.; Meschke, G.(Eds): *Lifetime-oriented Structural Design Concepts*, pp. 469–473. Springer.

Schrefler, B. (1995): F.E. in environmental engineering: coupled thermo-hydro-mechanical processes in porous media including pollutant transport. *Archives of Computational Methods in Engineering*, vol. 2, no. 3, pp. 1–54.

Simo, J.; Oliver, J.; Armero, F. (1993): An analysis of strong discontinuities induced by strain-softening in rate-independent inelastic solids. *Computational Mechanics*, vol. 12, pp. 277–296.

Snow, D. (1969): Anisotropic permeability of fractured media. *Water Resources Research*, vol. 5, pp. 1273–1289.

Stazi, F.; Budyn, E.; Chessa, J.; Belytschko, T. (2003): An extended finite element method with higher-order elements for curved cracks. *Computational Mechanics*, vol. 31, pp. 38–48.

Sukumar, N.; Chopp, D.; Moran, B. (2003): Extended finite element method and fast marching method for three-dimensional fatigue crack propagation. *Engineering Fracture Mechanics*, vol. 70, pp. 29–48.

Sukumar, N.; Moës, N.; Moran, B.; Belytschko, T. (2000): Extended finite element method for three-dimensional crack modelling. *International Journal for Numerical Methods in Engineering*, vol. 48, pp. 1549–1570.

Szabó, B.; Babuška, I. (1991): *Finite Element Analysis*. John Wiley & Sons, Inc.

van Genuchten, M. (1980): A closed-form equation for predicting the hydraulic conductivity of unsaturated soils. *Soil Science Society of America*, vol. 44, pp. 892–898.

Wells, G.; Sluys, L. (2001a): A new method for modelling cohesive cracks using finite elements. *International Journal for Numerical Methods in Engineering*, vol. 50, pp. 2667–2682.

Wells, G.; Sluys, L. (2001b): Three-dimensional embedded discontinuity model for brittle fracture. *International Journal of Solids and Structures*, vol. 38, pp. 897–913.

Xie, M.; Gerstle, W. (1995): Energy-based cohesive crack propagation modeling. *Journal of Engineering Mechanics (ASCE)*, vol. 121, no. 12, pp. 1349–1358.

Zi, G.; Belytschko, T. (2003): New crack-tip elements for X-FEM and applications to cohesive cracks. *International Journal for Numerical Methods in Engineering*, vol. 57, pp. 2221–2240.